Surfaces and Interfaces 74 (2025) 107657

Contents lists available at ScienceDirect

Surfaces and Interfaces

journal homepage: www.sciencedirect.com/journal/surfaces-and-interfaces

Rapid microwave hydrothermal synthesis of rare Earth-modified ZnO photocatalysts: Enhanced activity and comprehensive structural analysis

Otman Bazta [a,*], Juan Francisco Ramos-Justicia [b,c], Ana Urbieta [b], Susana Trasobares [a], Paloma Fernández [b], Jose Juan Calvino [a], Ana Belén Hungría [a]

[a] Department of Materials Science and Metallurgical Engineering and Inorganic Chemistry, University of Cadiz, Cadiz, Spain
[b] Department of Physics, Complutense University of Madrid, Madrid, Spain
[c] Laser Processing Group, Institute of Optics (IO-CSIC), C/Serrano, 121, Madrid, Spain

ARTICLE INFO

Keywords:
ZnO nanosheets
Surface decoration
Microwave-assisted hydrothermal synthesis
Charge separation efficiency
Nanostructured photocatalysts
Rare earth modification

ABSTRACT

This study demonstrates that, under the specific synthesis conditions applied, the addition of rare earth ions (Ce^{3+}, Y^{3+}, Eu^{3+}) to ZnO does not lead to their incorporation into the lattice as dopants but instead results in their surface decoration, as revealed by advanced nanoscale characterization.

ZnO and rare earth-modified ZnO photocatalysts (ZnO:RE = ZnO:Eu, ZnO:Y, ZnO:Ce) with a rare earth (RE) concentration of 2 at.% were synthesized via a rapid and environmentally friendly microwave-assisted hydrothermal method. The effect of adding different RE elements on the structural, morphological, and photocatalytic properties of the samples was systematically investigated. A thorough characterization was conducted using X-ray diffraction (XRD), field emission scanning electron microscopy (FESEM), high-angle annular dark field (HAADF)-scanning transmission electron microscopy (STEM), energy-dispersive X-ray spectroscopy (EDX), and photoluminescence spectroscopy (PL) at various excitation wavelengths and temperatures.

XRD analysis confirmed that all ZnO:RE samples retained the hexagonal wurtzite crystal structure of ZnO. FESEM images revealed that pure ZnO consisted of randomly distributed smooth nanosheets, while the addition of RE elements led to the formation of small particles dispersed over the nanosheet surfaces. A detailed structural analysis using STEM revealed that the rare earth elements formed structures decorating the surface of ZnO nanosheets rather than being fully incorporated into the ZnO lattice, indicating a dispersion of RE species over the ZnO matrix. This unique distribution significantly influenced the material's properties.

The photocatalytic performance of the ZnO:RE samples was evaluated through the degradation of methylene blue (MB), demonstrating superior activity compared to pure ZnO and TiO_2-P25. Among the modified samples, the cerium-modified ZnO (ZnO:Ce) exhibited the highest MB degradation efficiency. Furthermore, PL spectroscopy combined with TEM analysis provided critical insights into the relationship between defect characteristics and photocatalytic activity, offering a deeper understanding of the mechanisms driving performance enhancement. These findings highlight the potential of rare earth surface structures-ZnO nanosheets heterojunctions as a strategy for optimizing the photocatalytic properties of ZnO-based materials.

1. Introduction

Nowadays, semiconductor materials such as SnO_2, Bi_2O_3, WO_3, TiO_2 and ZnO, have gained significant attention for applications in luminescence, solar cells, gas sensors and UV-blocking [1–3]. Among these materials, TiO_2 and ZnO stand out for their favorable chemistry, low cost, and potential to replace traditional pollutant-removal methods (e.g., adsorption, biological degradation, chlorination, ozonation) [4–6]. ZnO has emerged as a promising candidate in this particular field due to its wide direct bandgap, as well as its low cost, non-toxic nature, and ease of surface modification, making it environmentally sustainable [7].

However, the industrial application of ZnO photo-catalyst faces two main limitations: (i) its large band gap of 3.37 eV at room temperature, making it primarily responsive to UV light. Since UV light constitutes only approximately 5 % of the solar spectrum, a significant portion of solar photons in the visible light (approximately 40 %) are not absorbed

* Corresponding author.
E-mail address: otman.bazta@uca.es (O. Bazta).

https://doi.org/10.1016/j.surfin.2025.107657
Received 7 July 2025; Received in revised form 18 August 2025; Accepted 10 September 2025
Available online 11 September 2025

[8,9]. Second, rapid recombination of photogenerated electron–hole pairs reduce its efficiency under UV–Vis illumination [10,11]. To overcome these limitations and enhance the efficiency of ZnO as a photo-catalyst under solar irradiation it is crucial to modify its bandgap and mitigate the recombination phenomena to facilitate visible light absorption.

In this context, extensive efforts have been made to modify ZnO properties to extend its response to visible light and increase the e^-/h^+ pairs lifetime. For example, doping using metals/nonmetals is an efficient process to adjust properties of ZnO to meet the needs for highly efficient applications [12–15]. Another approach involves constructing heterojunction photo-catalyst by combining different semiconductors, which has gained considerable attention for enhancing the lifetime of photo-generated electron-hole pairs [16–19]. Recently, there has been increasing research in rare earth elements modified ZnO. The addition of rare earth ions to ZnO was reported as an effective approach to enhance the photocatalytic response [20,21]. In this sense, rare earth elements contribute to modifying structural parameters such as crystallite size, surface defects, and consequently catalytic activity. In addition, rare earth ions can generate the intra-4f optical transition due to their partially filled 4f shell [22,23]. Doping with rare earth elements also provides means to stabilize the structure, preventing crystallite agglomeration and enhancing thermal stability of ZnO [24,25]. Several studies have been devoted to enhancing the light response of ZnO via integrating many rare earths as dopants. These elements appear to be very efficient to trap the photoinduced charge carriers and prevent the recombination process, as demonstrated in systems like Er-doped spherical-like ZnO [26,27], Eu modified ZnO nanoparticles [28,29] Ce-modified nanostructures [30] or Sm-doped ZnO nanorods [31].

Numerous studies have reported that the addition of rare earth ions in ZnO matrices can introduce significant surface defects which, in turn, enhance the photocatalytic performance of ZnO by promoting charge separation. However, contrasting reports have pointed out adverse effects of defects on the catalytic activity of ZnO [32,33]. Therefore, there are yet uncertainties concerning the role of different relevant structural parameters, whose clarification calls for further experimentation.

Many of these works assume that rare earth cations are incorporated into the ZnO lattice because no new phases are observed in the X-ray diffraction patterns. However, nanoscale characterization of these materials using electron microscopy techniques allows for the identification of these new phases, which may be present in very small quantities, below the detection limit of X-rays [34].

In this study, our main objective is to analyze the influence of incorporating different rare earth cations on the photocatalytic response of ZnO systems. We will approach this question by examining the influence of this modification on the structural properties, including the formation of different types of defects, as well as on their charge carrier dynamics. To achieve this goal, we have prepared different photocatalysts based on ZnO which were modified with a fixed amount of RE metal ions (2 at %) via a microwave-assisted hydrothermal method. A fixed doping level of 2 atomic percent (at %) of rare earth (RE) metal ions was chosen based on previous reports indicating this concentration as optimal for enhancing photocatalytic activity while minimizing excessive lattice distortion or secondary phase formation. This synthesis technique enables the production of well-controlled nanostructures within short reaction times under uniform heating conditions. Additionally, the microwave-assisted method provides a cost-effective approach, as its high yield ensures efficient utilization of precursor materials [35].

Building on these advancements and in comparison, to studies that have developed ZnO-based photocatalysts [36–38] demonstrating improved activity under UV or visible light. Our work complements these efforts by introducing a microwave-assisted hydrothermal syntheses that is faster and more energy-efficient, by evaluating performance under solar-simulated irradiation, and by providing nanoscale (STEM, EDX, TEM) and post-use (XRD, TEM) characterization to confirm surface decoration and long-term stability. Together, these features underscore the practical applicability and mechanistic clarity of our RE-modified ZnO photocatalysts for real-world pollutant degradation.

2. Experimental

2.1. Photocatalyst preparation

The materials employed for the preparation of RE-doped ZnO were of analytical grade without further purification. The pure ZnO and ZnO:RE samples with 2 % at. RE in the cationic fraction were synthesized by a microwave-assisted hydrothermal method. The procedure followed for pure ZnO preparation was as follows: 6 g of zinc acetate dihydrate ($Zn(O_2CCH_3)_2(H_2O)_2$) and 4 g of hexamethylenetetramine (HMT, $(CH_2)_6N_4$) were dissolved in 100 mL of MQ water. Then, 0.3 M aq. NaOH solution was added dropwise into the above solution and stirred continuously for 1 h at room temperature (pH = 10). The resultant milky mixture was transferred and sealed in two 100 mL Teflon-lined autoclave vessels, placed into the reactors and then heated up to 180 °C in a microwave oven with a controlled power of 400 W for 18 min. The white precipitates formed were centrifuged and thoroughly washed by repeated centrifugation – redispersion with MQ water and then absolute ethanol. The white precipitates were collected and dried in an air oven maintained at 110 °C for 12 h. A similar procedure was followed to prepare the samples modified with a 2 % at. Y, Ce or Eu using the corresponding amounts of the nitrate precursors. All rare earth (RE) nitrate precursors used in this work were purchased from Sigma-Aldrich, with a stated purity of 99.99 %. These precursors ($Y(NO_3)_3$, $Ce(NO_3)_3$, and $Eu(NO_3)_3$) were fully dissolved as RE^{3+} ions (Y^{3+}, Ce^{3+}, Eu^{3+}) in the reaction solution. TiO_2-P25 from Evonik was used as a reference for the photocatalytic activity tests.

2.2. Characterization details

The XRD patterns of ZnO and RE modified ZnO were recorded using Bruker D8 advance X-ray diffractometer in the 20°−80° 2θ range with λ = 0.154056 nm. Surface morphology of the crystallites was examined by scanning electron microscopy (SEM, Nova NanoSEM 450). Transmission Electron Microscopy (TEM) was performed with a TEM/STEM system (FEI Talos F200X) equipped with 4 Super-X SDDs. HAADF-STEM images and XEDS maps were acquired using a high brightness electron probe in combination with a highly stable stage which minimized sample drift. Element maps were acquired with a beam current of 100 pA, a dwell time of 50 μs was used, resulting in a total acquisition time of approximately 12 min.

Optical absorption spectra of pure and modified ZnO were recorded on a Shimadzu UV- 1603 UV–Visible spectrophotometer. Ethanol absolute was used as the reference medium. The optical bandgap was determined by analyzing the first derivative of the absorption spectrum (dα/dE). This method identifies transition energies directly from derivative peaks, resolving weak excitonic features and overlapping transitions that conventional Tauc plots may miss [39–41].

The photoluminescence (PL) spectra were recorded either on a confocal Horiba Jobin Yvon Labram HR 800 with excitation at 325 nm or using a photoluminescence spectrometer FLS 1000 (Edinburgh Instruments), where the samples were excited by a continuous 450 W Xe lamp and the photoluminescence was detected by a Hamamatsu R928P photomultiplier detector. All the spectra were corrected for the instrument response. The near-band edge peak positions were obtained by numerical fitting of the PL spectra to determine the maxima with higher accuracy than visual inspection of the raw spectra.

2.3. Photocatalytic activity

The photocatalytic activity of the different samples was evaluated by studying the degradation of methylene blue dye (MB). For each

experiment, 100 mg of sample was dispersed in 300 mL of a 10 mg/L MB solution, a concentration selected based on commonly adopted values in photocatalytic studies to ensure comparability with literature while providing optimal conditions for accurate spectrophotometric monitoring without saturation or self-shielding effects. No sacrificial agent was added, as the study focused on evaluating the intrinsic photocatalytic activity of the materials under solar-like irradiation. The resulting mixture was stirred magnetically for 60 min in complete darkness to attain the adsorption-desorption equilibrium of MB onto the photo-catalyst.

Cold water was continuously supplied through a water circulating jacket to maintain the reaction temperature below 25 °C. A xenon immersion lamp (model TXE150, UV-Consulting Pechl), emitting radiation comparable to solar spectrum, was fully submerged in the reaction solution in a zero-distance configuration to ensure direct and uniform light exposure without air gaps. Aliquots (5 mL) were withdrawn every 15 min, centrifuged (10 min, 5000 rpm), and the absorbance variation at λ_{max} was monitored.

For recyclability tests, the catalyst was harvested by centrifugation after each cycle, air-dried, re-weighted, and re-dispersed in fresh MB solution for subsequent activity tests (up to 4 cycles) following the same adsorption equilibrium procedure.

The photocatalytic efficiency (PE) of different photo-catalysts for the degradation of MB was estimated using the following formula.

$$PE\ (\%) = \left(1 - \frac{C_t}{C_0}\right) x100\% \quad (1)$$

In which, C_0 corresponds to the initial concentration of MB dye after adsorption-desorption, and C_t represents the concentration of MB at different times. Blank experiments without adding any catalysts were also performed to discard MB self-photolysis.

3. Results and discussion

3.1. Structural analysis

X-ray diffraction (XRD) analysis was conducted to investigate the crystal structure and estimate the average crystallite size of both pure ZnO and rare earth (RE)-modified ZnO samples. Fig. 1a presents the XRD patterns of all synthesized materials. The diffraction peaks observed in all samples correspond to the hexagonal wurtzite phase of ZnO (JCPDS No. 36–1451) [42], with no additional peaks attributable to secondary phases. Upon closer examination of the (101) region Fig. 1b, we do observe a slight shift in peak position for the RE-modified ZnO samples most pronounced for ZnO:Ce consistent with local lattice distortion or strain induced by surface decorated RE species. However, complementary HAADF-STEM and EDX analyses confirm that these elements form discrete surface domains rather than uniformly substituting into the ZnO lattice, indicating that the observed shift arises from interfacial interactions rather than classical substitutional doping. Furthermore, the presence of intense and sharp peaks suggests high crystallinity in all samples, underscoring the quality of the synthesized materials.

The surface area is a key factor influencing photocatalytic activity, as a higher surface area provides more active sites for pollutant adsorption. We determined the BET surface areas of pure and RE-modified ZnO nanoparticles from N_2 adsorption–desorption isotherms; the corresponding isotherms and calculated surface area values are provided in the Supporting Information (Fig S1).

The average crystallite size of all samples was obtained by means of Debye Scherrer Formula:

$$D = \frac{0.9\lambda}{\beta\cos\theta} \quad (2)$$

Where D, λ, θ and β correspond to the effective crystallite size, X-ray wavelength, Bragg's diffraction angle and full width at half maximum (FWHM) respectively. The numerical values were obtained using the most intense peak (101). The average crystallite size of pure ZnO was found to be higher than that of the modified ZnO as shown in Table 1. The reduction in crystallite size observed in RE-modified ZnO is attributed to the formation of RE-O-Zn linkages on the surface of the modified samples, which likely inhibit crystal grain growth [43]. This smaller crystallite size increases the surface area, allowing for greater adsorption of pollutants onto the catalyst surface which could likely have a beneficial effect on the catalytic activity.

Table 1
Calculated values of crystallite size of the prepared samples.

Photocatalyst	ZnO	ZnO:Eu 2 %	ZnO;Ce 2 %	ZnO:Y 2 %
Crystallite size (nm) ± 1 nm	45	35	29	35

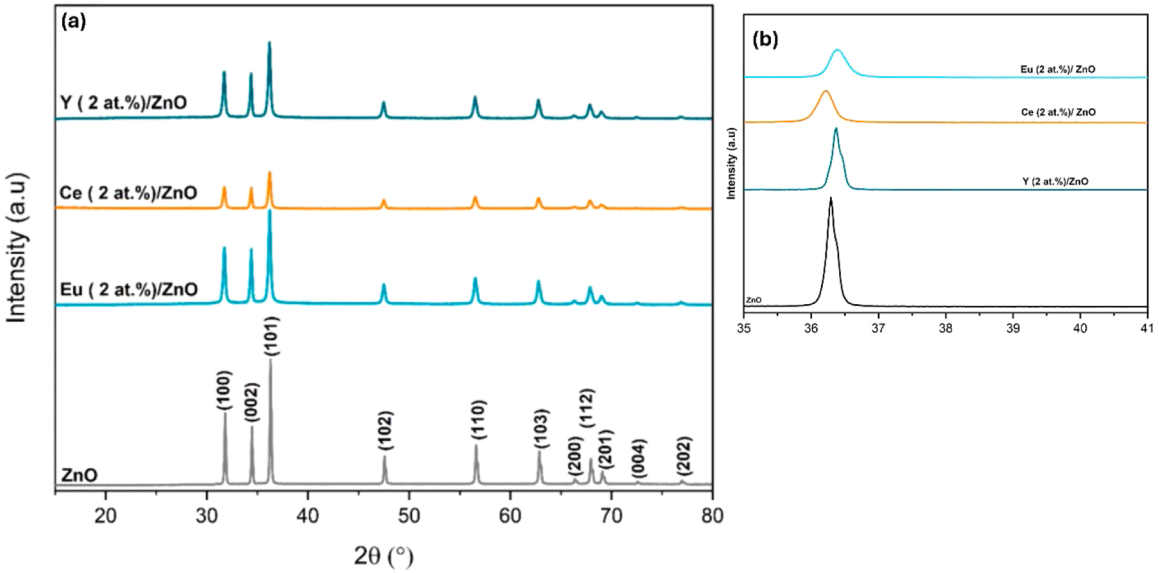

Fig. 1. (a) XRD patterns of ZnO and ZnO:RE samples (b) Zoom on the (101) peak region.

3.2. Morphological and compositional analysis

The surface morphology of the pure (ZnO) and modified (Eu, Ce or Y) were characterized using scanning electron microscopy (SEM). The SEM images shown in Fig. 2 revealed the formation of plates with varying diameters ranging from 200 to 600 nm. These plates exhibited a relatively consistent thickness of 25 to 50 nm.

When a second element (Eu, Ce, or Y) was added into the ZnO composition, slight changes in the surface appearance of the sheets were observed. Aggregates of much smaller size were noticed, which may be related to the presence of a secondary phase in the modified ZnO samples. Considering the small amount of the second element introduced into the catalyst formulation, the quantity of this secondary phase is so small that it is not detectable by XRD.

To provide a comprehensive morphological and compositional characterization of the samples, a detailed analysis was performed by Scanning Transmission Electron Microscopy (STEM) recording both images in High-Angle Annular Dark Field (HAADF) mode and X-EDS elemental maps. In HAADF images, the contrast is directly related to both the sample's thickness and the atomic number of the elements present in the imaged areas. This allows for the visualization and differentiation of various structural features and chemical elements in the samples.

Fig. 3 shows representative STEM-HAADF images of each of the samples. These STEM-HAADF images provided further confirmation of the observations made using SEM, but with higher resolution and finer details. The samples are composed of nano-sheets which in the case of samples with a second element also have areas with different morphology, that are highlighted in the images with a white square. These regions depict different structural characteristics and elemental composition. In the case of Europium, they appear as small rods and in the case of cerium and yttrium, as agglomerates of small particles.

To perform a quantitative analysis of the composition of a given area of the sample, either the electron beam can be stopped at any point of interest and acquire a spot-type XED spectrum, or more efficiently for this type of materials, an area can be delimited and a XED spectrum can be recorded on each of the pixels contained in that region. Each of these spectra can be processed and images can be formed in which the pixels containing a certain element are colored with a specific color code for that element. Furthermore, with the collected XED spectra, it is also possible to quantify the elements present in any part of the mapped area. This quantitative analysis provides valuable information about the elemental composition and allows for a deeper understanding of the distribution and concentration of elements in the sample.

In the analysis of the ZnO sample, Fig. 4(a) presents a HAADF-STEM image. The image showcases a porous sheet with a length of up to half a micron and a width of approximately 300 nm. Additionally, several sheets are visible in the profile view, exhibiting a thickness of about 50 nm. Fig. 4(b) corresponds to the elemental map of the same area, obtained through X-ray energy-dispersive spectroscopy (XEDS). In this map, only the presence of Zn cations is identified, which is expected for an unmodified ZnO sample. The spectrum shown in Fig. 4(c) represents the entire analysed area and includes the signals from various elements. It displays characteristic lines corresponding to copper (originating from the grid), carbon (from the holey carbon film on which the sample is deposited), oxygen, and zinc (from the sample itself).

The compositional analysis of the samples modified with europium, cerium and yttrium provides very interesting results. Firstly, a representative analysis of the ZnO:Eu 2 % sample is shown in Fig. 5. The HAADF-STEM image presented in Fig. 5a shows a typical porous ZnO plate on which elongated, about 100 nm long and 20 nm wide, also porous structures are deposited. When the composition of this zone is studied by means of XEDS, it can be seen that the small rods are mainly composed of europium, which are shown as purple areas in Figs. 5(b) although small amounts of zinc, around 5 %, can also be quantified. However, the large sheets contain mainly zinc as shown in Fig. 5(b). In

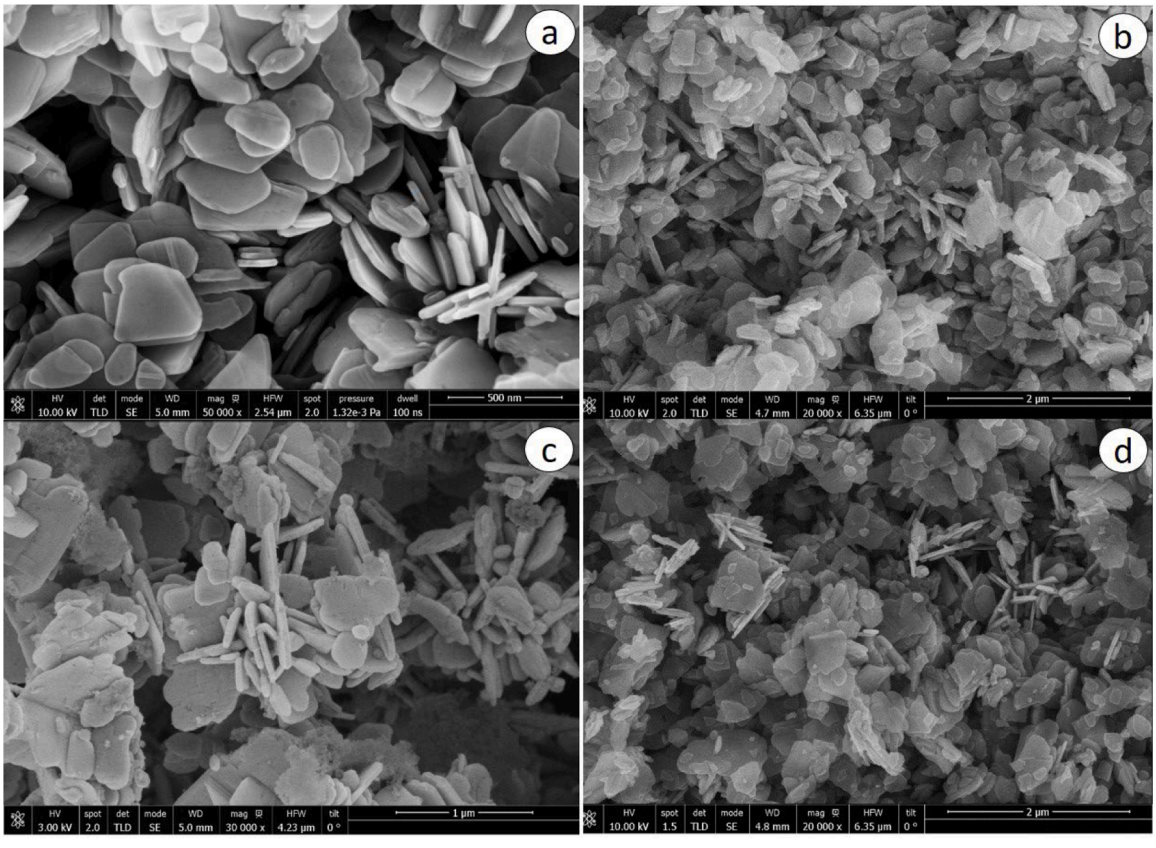

Fig. 2. SEM images of samples (a) ZnO, (b) ZnO:Eu 2 %, (c) ZnO:Ce 2 % and (d) ZnO:Y 2 %.

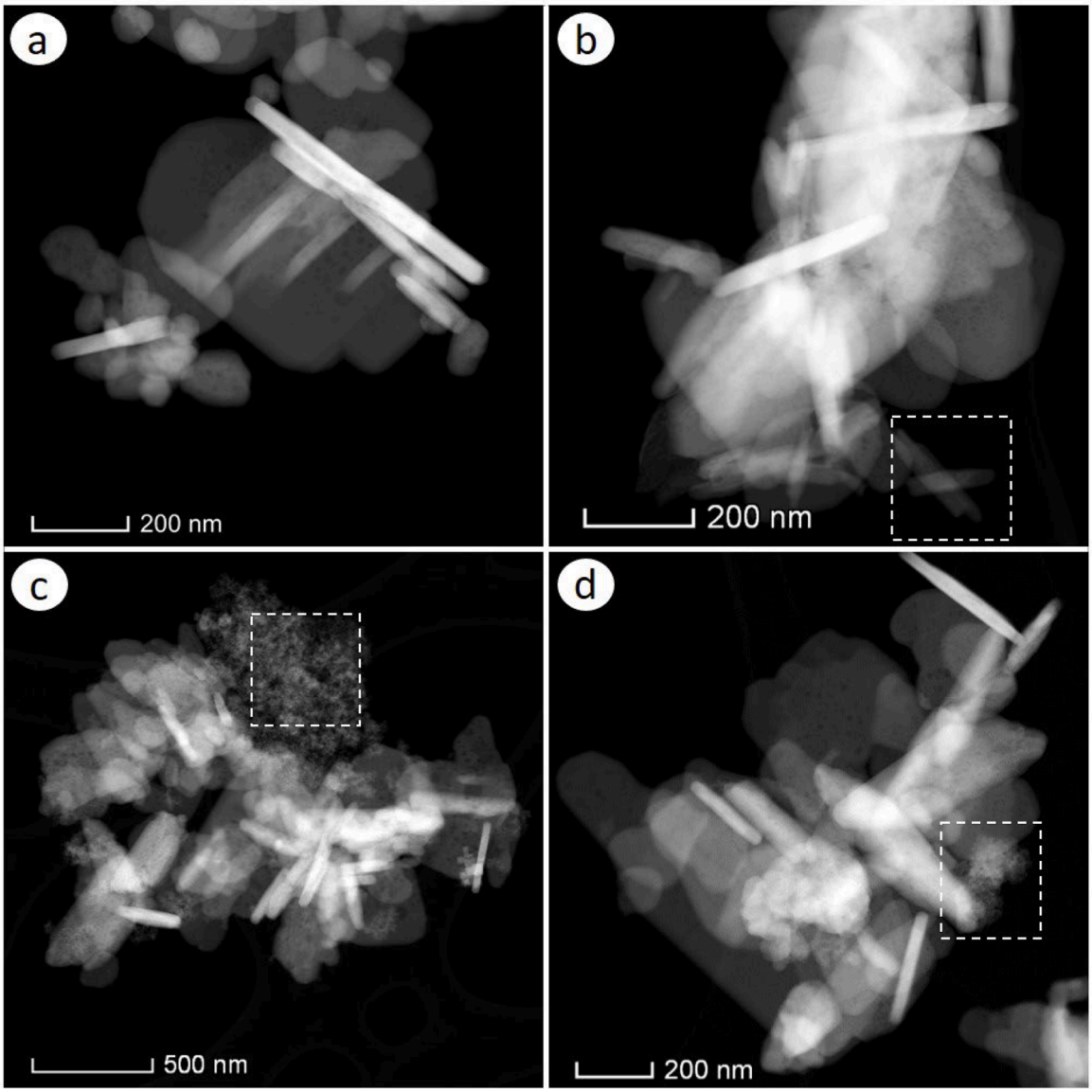

Fig. 3. STEM HAADF images of samples (a) ZnO, (b) ZnO:Eu 2 %, (c) ZnO:Ce 2 % and (d) ZnO:Y 2 %.

fact, the amount of europium detected in these areas, below 0.1 %, can be considered as an artifact due to noise from the spectrum background. Therefore, from the analysis of a large set of experiments like the one shown in Fig. 5, ZnO:Eu 2 % sample consists of two different components, pure ZnO plates onto which nanorods with an average composition of $Eu_{0.95}Zn_{0.05}O_x$ are deposited.

For the cerium-modified sample, a similar situation is observed, albeit with certain distinctions compared to the europium-modified sample. As previously mentioned and evident in the HAADF-STEM image shown in Fig. 6(a), the sample is composed of nano sheets onto which accumulations of cerium-rich nanoparticles are deposited in a non-uniform way. Quantification of the chemical composition of the aggregates, Figs. 6b, evidence that they contain an appreciable amount of zinc. In fact, they correspond to a $Ce_{0.7}Zn_{0.3}O_x$ mixed oxide as can be observed in the XEDS spectra quantified in Fig. 6(c). As in the europium-modified samples, the plate-shaped crystallites correspond to pure ZnO, as shown in XEDS in Fig. 6(d).

Finally, the analysis of the yttrium-modified sample reveals, as in the case of ZnO:Ce 2 %, the presence of yttrium-rich nanoparticles heterogeneously supported on the ZnO plates, as can be seen in Fig. 7(a,b). However, when the composition of these nanoparticles is analyzed, it is observed that they also have small amounts of Zn, Fig. 7(c). In average, the stoichiometry of these nanoparticles is $Y_{0.95}Zn_{0.05}O_x$. As in the case of the europium and cerium-modified samples, the yttrium in the ZnO plates remains at noise level, Fig. 7(d). High-resolution microscopy analysis of the nanostructures formed from the different rare-earth elements is shown in Figures S2 to S4 of the supporting information, evidencing in all cases the presence of the corresponding rare-earth oxides.

To ensure the representativeness of the data discussed in the main manuscript, additional X-ray energy-dispersive spectroscopy (XEDS) maps for each individual sample are included in the supporting information (Figs S5 to S7).

4. Photoluminescence studies

Luminescence studies have been extensively used to investigate the incorporation of dopants into ZnO [44–46] and its effect on the defect structure of the material. PL spectra of all the samples have been measured from 5 to 285 K in 20 K steps, but the more significative ones are those at 5 K and 285 K (room temperature, RT), which are shown in Fig. 8. Fig. 8a shows PL spectra of the samples at 5 K. In all samples, two

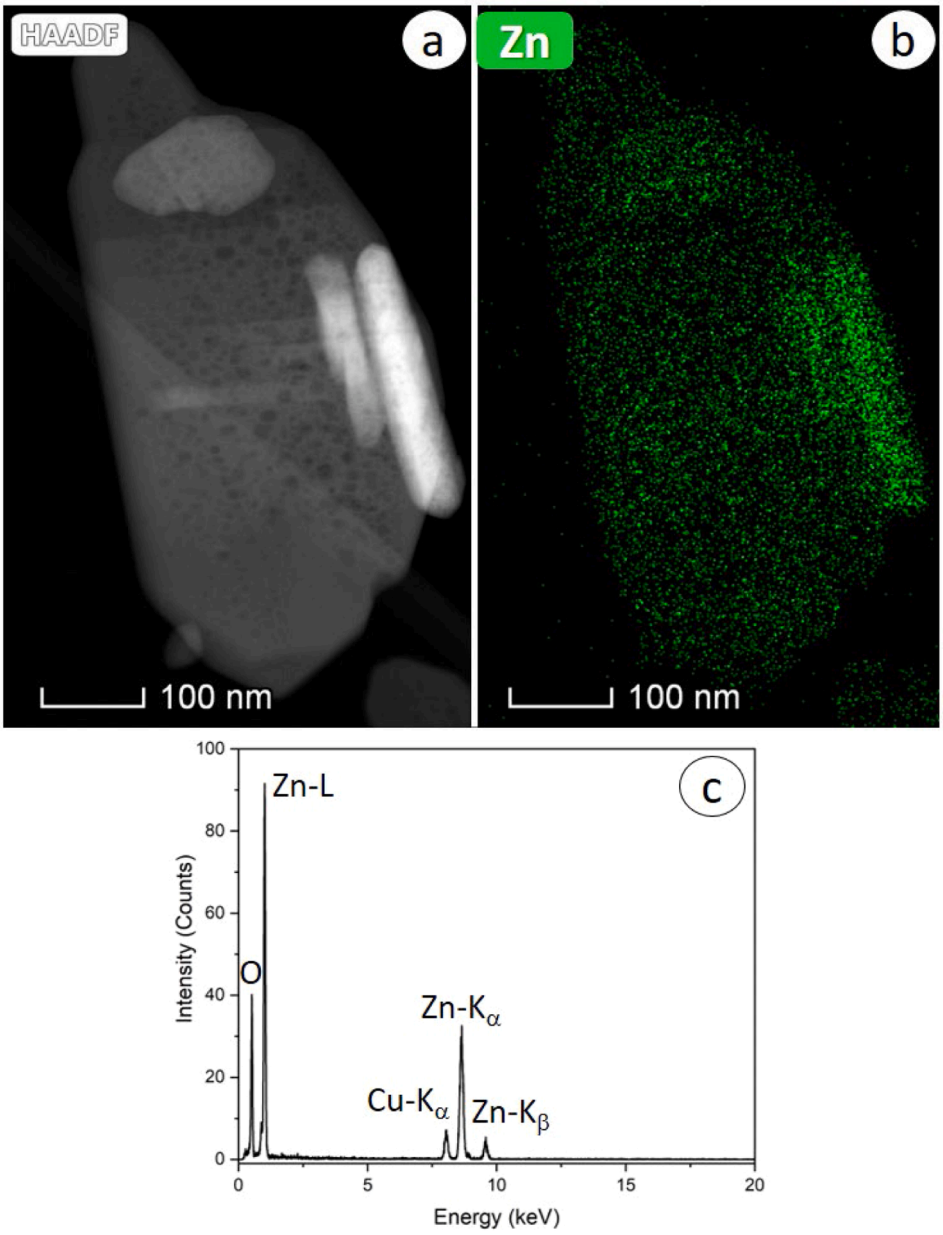

Fig. 4. (a) HAADF-STEM image, (b) XEDS elemental map showing the spatial distribution of Zn corresponding to the area displayed in (a), (c) XED spectra of the area displayed in (a).

clear bands are resolved: one whose peak lies in 3.369 eV, attributed to near-band edge of zinc oxide in the literature [47], and another wide one centred around 2 eV, normally ascribed to lattice defects [48]. The near-band edge band is left-shifted from its centre as a tail, possibly due to surface states generated by the dispersion on the size of the nanoparticles. Besides, the existence of shallow donors can also introduce energy levels close to near-band edge that can lead to luminescence emissions in this region. On the other hand, the visible band is alike for all samples except for their intensity. The visible band of ZnO pure nanoparticles is barely observed compared to the others, indicating a higher defect content in modified nanocrystals. The formation of vacancies or other native defects would be required to compensate the excess of charge leading to the observed increase of the intensity in the defect related emission bands. A more careful inspection of the visible band of ZnO:Eu shows that this band has shoulders at 1.8, 1.88, 2, 2.08, and 2.25 eV. The 2 and 2.08 eV peaks are ascribed to ionized vacancies and neutral vacancies, respectively [48,49]; 1.88 eV peak is attributed to zinc vacancies [50]. 2.25 eV peak is usually associated with deep level defects [51,36]. Although not as clear as in the Eu modified sample, the rest of the samples show the same emissions associated with intrinsic defects. These variations indicate a certain degree of incorporation of the dopants, however, as XED spectra show, their concentration in ZnO nanocrystals is very low, below the detection limit of the technique. In addition, the intraionic transitions of Eu are located at 1.75, 1.96 and 2.02 eV [52], that can be also included in the wide visible band, however, for the other samples, no direct evidence of dopant-related emissions into the lattice are observed in the luminescence spectra since all bands may be ascribed to intrinsic defects or near-band edge of ZnO [53].

In Fig. 8b, a significant effect of temperature is observed. The near-band edge is redshifted, as expected, since the thermal activation helps to reduce the effective gap between valence and conduction bands. In addition, it varies slightly depending on the sample. The maxima of the peaks are collected in Table 2. Except for ZnO, the difference in

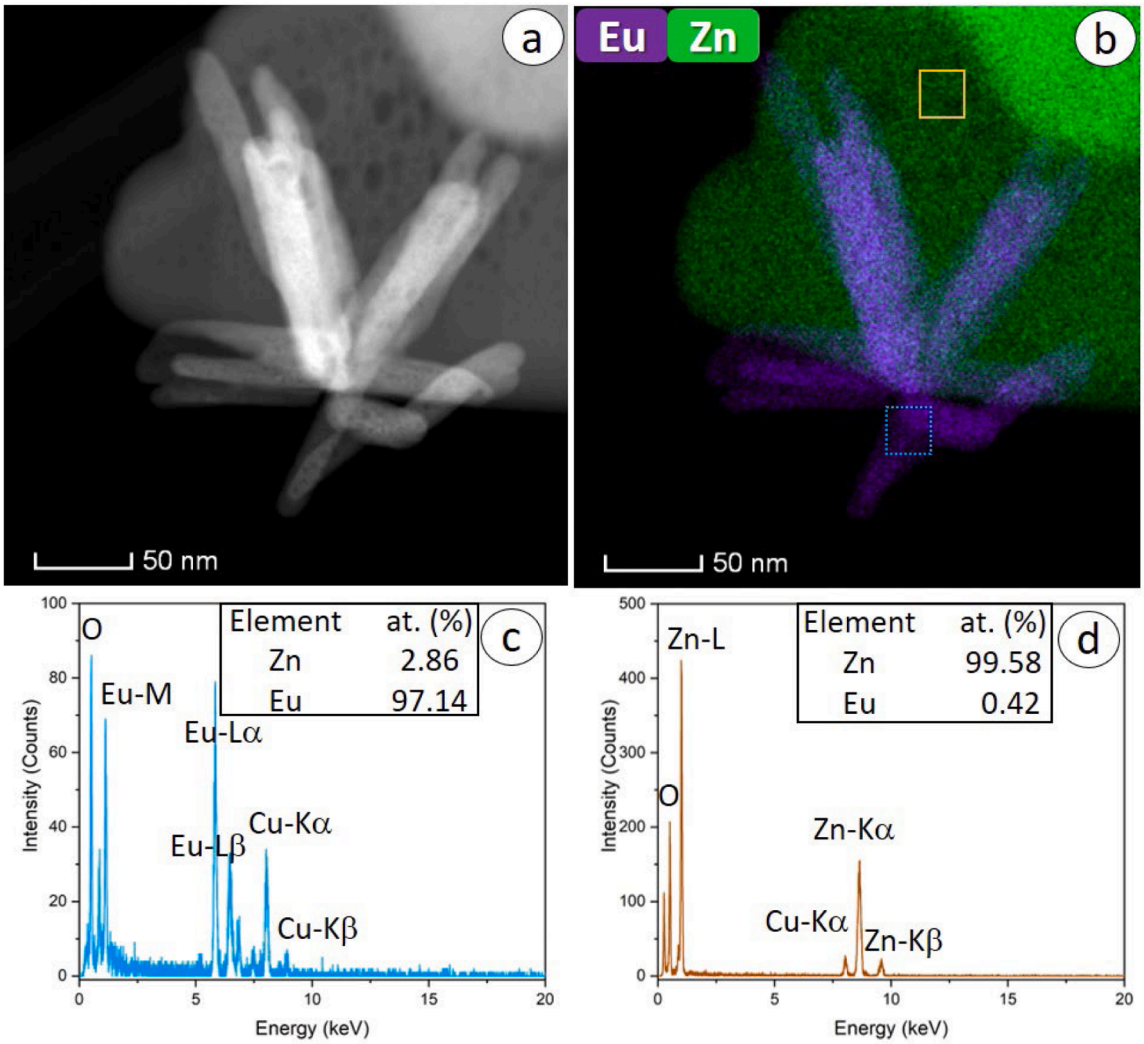

Fig. 5. Sample ZnO:Eu 2 %. (a) HAADF-STEM image, (b) XEDS elemental maps showing the spatial distribution of Eu (purple) and Zn (green). (c) XED spectra of the area marked in blue in (b). (d) XED spectra of the area marked in yellow in (b).

relative intensities in the rest of the samples is reversed, what suggests two ideas: temperature activates non-radiative mechanisms which diminish the relative intensity of the near-band edge; or dopants enhance certain luminescence mechanisms on the visible band at the expense of the near-band edge one. The ZnO visible band is centred at 2.25 eV, and the other are centred around 2.1 eV. These peaks were observed before at low temperature, so the efficiency of each contribution may be dependent on the activation energy of the mentioned defects, and not on the selected dopants. No changes in the spectra recorded on the modified samples at 5 and 295 K are observed, indicating a faint influence of added elements in the PL emission. As known, intraionic transitions are independent on temperature; if dopants were incorporated to the lattice, characteristic peaks at the same temperature as 5 K would be observed at RT. If yttrium played a significant role, its green band would also be flatter than the rest at RT, a not observed fact. The spectra of ZnO:Y and ZnO:Eu are already the same at RT, which may be indicative of the absence of Eu. The same argument could be applied to ZnO:Ce. These observations lead us to conclude that while the dopants are present, they are not incorporated into the lattice. This conclusion is supported by the absence of their typical features in the PL spectra at any temperature.

The dependence of the optical bandgap with the temperature can be also investigated. Fig. 9 shows the relationship between these two variables and its fitting to Varshni's relation [54]:

$$E_{gap}(T) = E_{gap}(0) - \frac{\alpha T^2}{T+\beta},$$

where α and β are typical constants characteristic of each material, and $E_{gap}(0\ K)$ is the theoretical value of the near-band edge at absolute zero. As can be seen, the fit to the experimental data is good, and the theoretical value of the near-band edge is given in the Table 3. Although only ZnO:Y experimental near-band edge is compatible with the range given in Table 1, it should be taken into account that our measurements were taken at 5 K. As the divergence on the theoretical values and the experimental is minute and, bearing in mind that those last ones are in consonance with the literature [47–50], we can conclude that the obtained discrepancy is not significant. Nevertheless, the interval of energies of theoretical near-band edges overlaps with some of the samples, in particular, with pure ZnO, suggesting that the bandgap shift is not caused by the incorporation of dopants in agreement with the above-mentioned observations.

Fig. 10 shows the optical absorption spectra of the samples at room temperature. It is well known that ZnO is a direct-gap semiconductor [55], which is reflected on the absorption spectra of all samples by a sharp, increasing line when the optical bandgap is reached. The determination of the optical bandgap has been done by computing the derivative of the absorption spectrum, that will show a maximum at the optical bandgap position [56]. The numerical derivative is plotted on

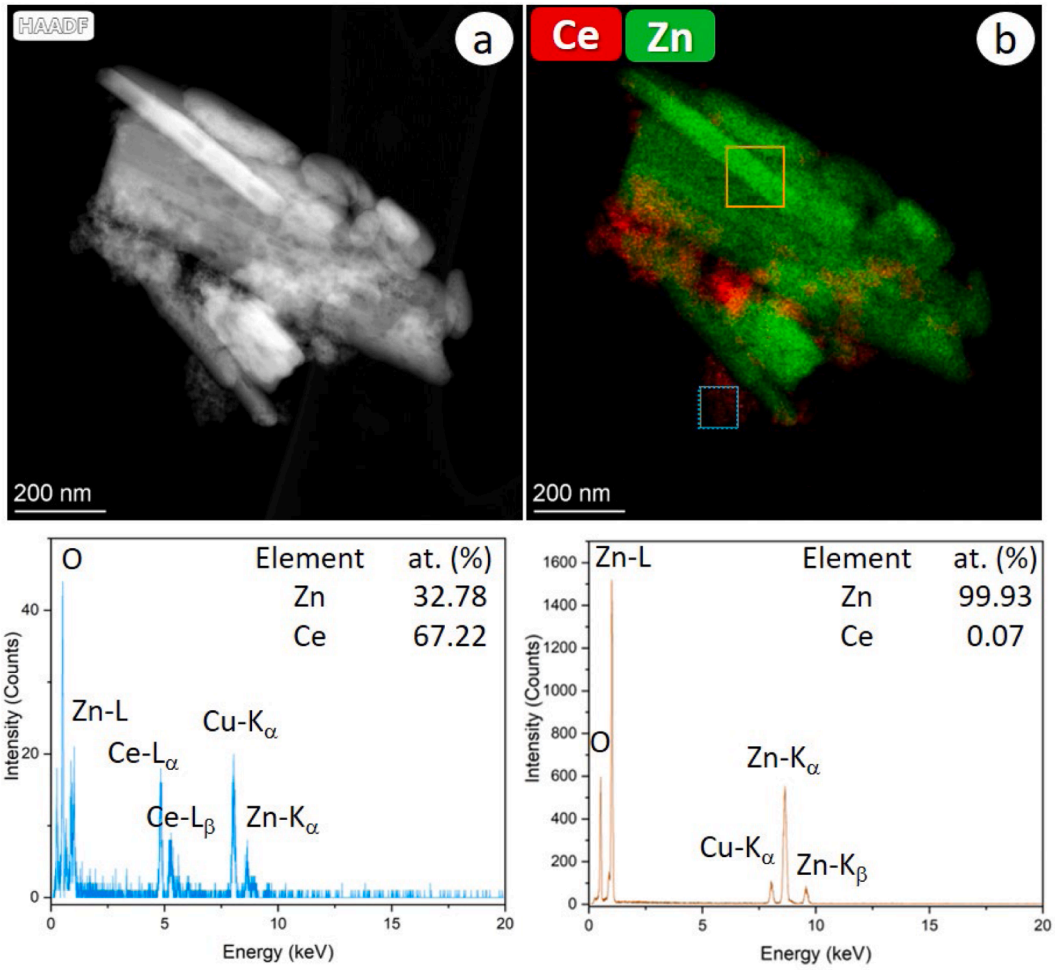

Fig. 6. Sample ZnO:Ce 2 %. (a) HAADF-STEM image, (b) XEDS elemental map showing the spatial distribution of Ce (red) and Zn (green) (c) XED spectra of the area marked in blue in (b). (d) XED spectra of the area marked in yellow in (b).

the inset of the Fig. 10, whose maxima are marked with a dashed vertical line, and whose maximum values at RT are summarized in Table 4. The calculated optical bandgaps fully coincide with experimental data, and their proximity may also suggest that RE have no effect on the bandgap energy.

5. Photocatalytic activity of RE-modified ZnO

The photodegradation rates of methylene blue (MB) using ZnO, ZnO:RE, and commercial TiO_2-P25 photocatalysts under simulated sunlight illumination are depicted in Fig. 11. The evaluation of the synthesized samples commenced by analyzing their MB degradation efficiency under identical experimental conditions. A negligible self-degradation of MB was observed in the absence of any catalyst, confirming that both the light source and the catalysts are indispensable for initiating the transformation of MB.

The modified ZnO samples exhibited a remarkable enhancement in MB degradation efficiency compared to both pure ZnO and P25. This superior performance can be attributed to several critical factors. Extensive research has shown that the formation of interfacial heterostructures, such as heterojunctions, facilitates more efficient charge separation and transfer at the interface, thereby minimizing electron-hole recombination [57–59]. For instance, Zhao et al. demonstrated that coupling ZnO with cerium not only broadens the spectrum absorption but also significantly improves charge separation efficiency. Similarly, Zhang et al [60]. revealed that the concentration of oxygen vacancies in ZnO—CeO_2 hybrids can be precisely tuned by adjusting the nitrogen atmosphere during synthesis, with the synergistic effect between ceria and oxygen vacancies enhancing the optical response and boosting photocatalytic activity for Rhodamine B (RhB) degradation. In a related study, Rodionov et al [61]. explored the incorporation of europium as a coating material on ZnO for dye degradation, attributing the improved performance to the enhanced stability, mechanical strength, and transparency of the coatings, which collectively optimize the spectral response and photocatalytic efficiency.

The most active sample, ZnO:Ce, was subjected to four consecutive cycles to evaluate its recyclability and stability as a photocatalyst. Specifically, the recyclability tests were conducted using MB as the target pollutant under consistent experimental conditions. After each cycle, the sample was recovered via centrifugation, followed by air drying for reuse. The results, as illustrated in Fig. 12, reveal exceptional stability in the photocatalytic degradation efficiency of the model molecule, underscoring the sample's robust reusability and potential for practical applications. Evidence for the morphological, structural, and compositional stability of the samples subsequent to the various catalytic runs is provided by XRD and XEDS-STEM analyses, depicted in Figures S8 and S9 of the supporting information.

In addition, the kinetics of MB dye degradation over ZnO, P25 and ZnO:RE photocatalysts were analyzed in terms of the Langmuir-Hinshelwood mechanism, a model widely employed to describe the relationship between the starting photo-degradation rate and initial concentration of reactant [62,63].

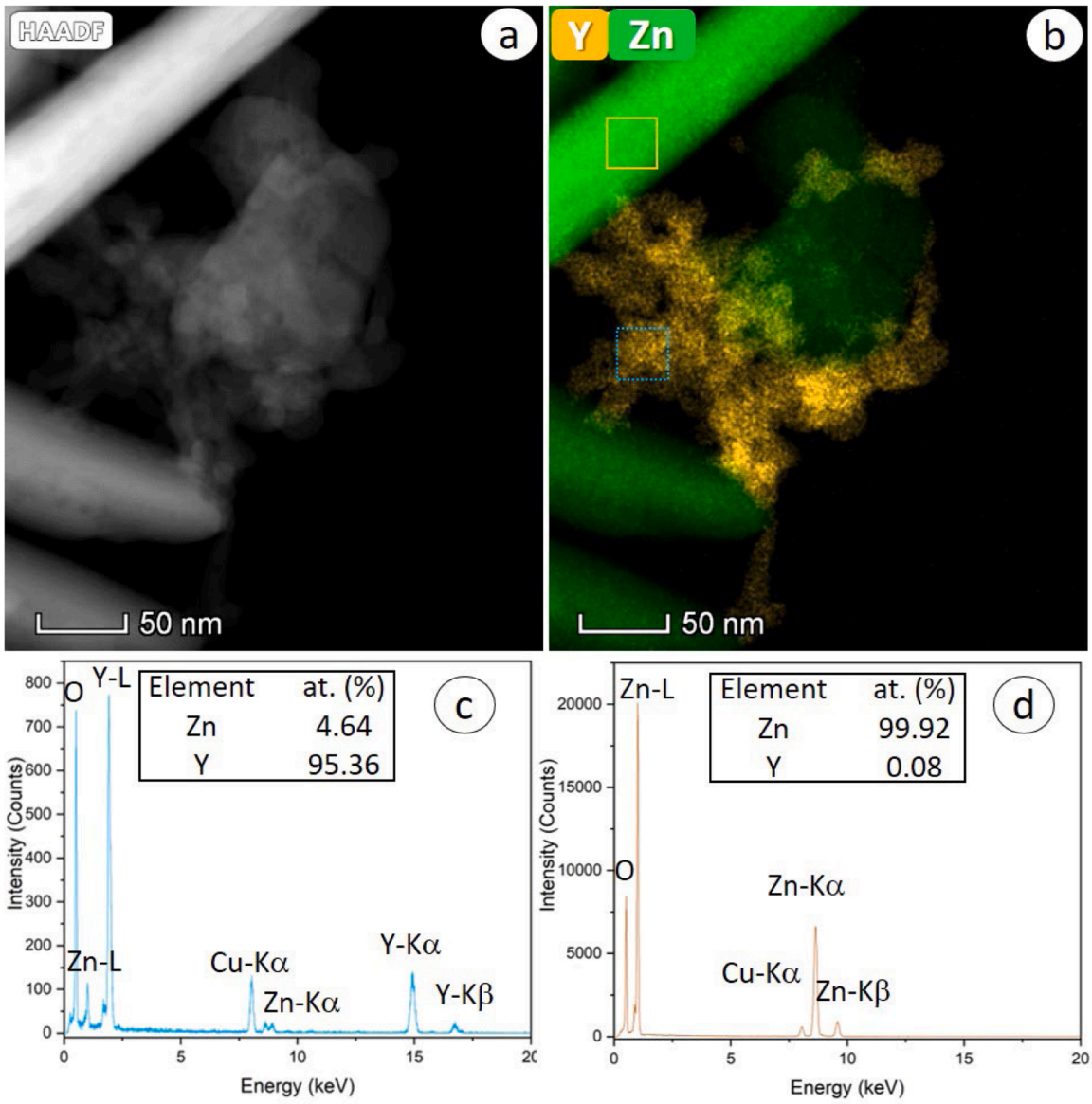

Fig. 7. Sample ZnO:Y 2 %. (a) HAADF-STEM image, (b) XEDS elemental map showing the spatial distribution of Y (yellow) and Zn (green). (c) XED spectra of the area marked in blue in (b). (d) XED spectra of the area marked in yellow in (b).

$$r = -\frac{dC}{dt} = \frac{k_r k_{ad}\, C}{1 + C k_{ad}}$$

Where, k_r represents an intrinsic rate constant, k_{ad} an adsorption constant and C the reactant concentration. Fig. 13 shows the plots corresponding to the integrated ($\ln(C_0/C)/(C_0-C)$ vs $t(C_0-C)$) form of the LH model, obtained MB photodegradation process by P25, ZnO and ZnO: RE photocatalysts. From the figure it is evident that all the photodegradation essays can be nicely fitted to the l-H model. The numerical values of the apparent constant rates after fitting are summarized in Table 5. The photocatalytic efficiency of the ZnO:RE photocatalyst was higher than ZnO and P25. the ZnO:Ce displayed a maximum degradation of about 95 % Fig. 13.

Overall, the photocatalytic degradation kinetics of methylene blue (MB) using ZnO, P25, and RE-modified ZnO catalysts were effectively described by the Langmuir–Hinshelwood model, as evidenced by the linearity of the fitting curves in Fig. 13. The derived apparent rate constants clearly demonstrate that all RE-modified ZnO systems exhibit significantly enhanced photocatalytic activity compared to both pure ZnO and commercial TiO_2-P25. In particular, the Ce-modified ZnO catalyst achieved the highest rate constant (12.03×10^{-2} M·min^{-1}), representing a nearly 20-fold increase over P25 and resulting in ~95 % MB degradation. Although the kinetic analysis was based on a single measurement per sample, the observed trends are consistent and indicative of the superior reactivity imparted by rare-earth surface modification. These results underline the effectiveness of RE/ZnO materials, especially ZnO:Ce, as efficient and rapid photocatalysts under solar-simulated irradiation.

6. Conclusions

This study provides novel insights into the interaction of rare earth (RE) elements with ZnO nanostructures, demonstrating, under specific synthesis conditions, that contrary to the common assumption of lattice doping Ce, Y, and Eu predominantly form surface-decorated nanodomains on ZnO nanosheets rather than substituting into the crystal lattice. ZnO and ZnO:RE (2 at. % Eu, Y, Ce) photocatalysts were synthesized via a rapid, energy-efficient microwave-assisted hydrothermal route and systematically evaluated.

XRD confirmed the retention of the hexagonal wurtzite phase and

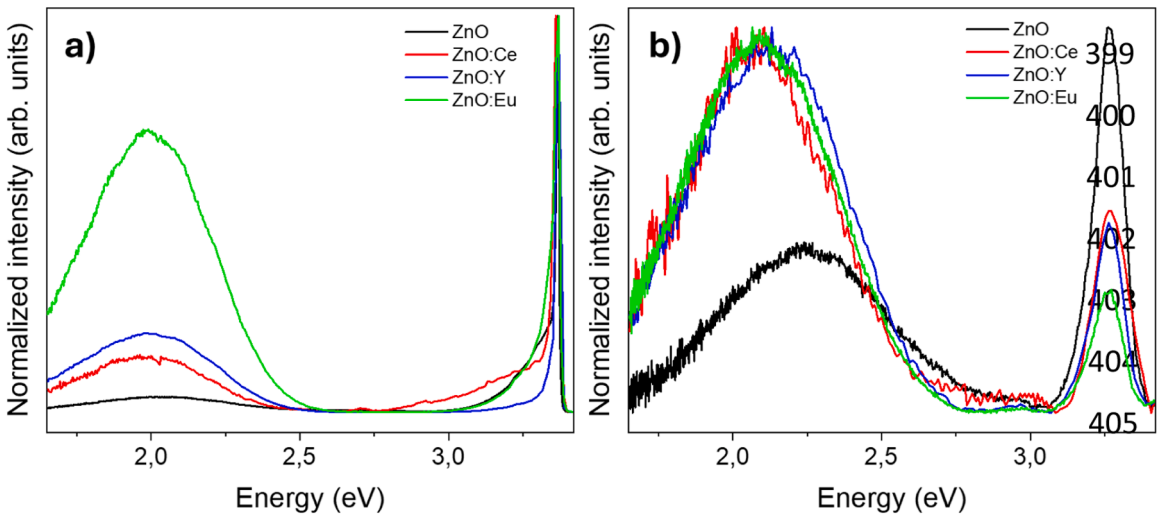

Fig. 8. PL spectra of all samples at: (**a**) 5 K; (**b**) 285 K (room temperature, RT).

Table 2
Near-band edge of the samples at 285 K.

	ZnO	ZnO:Ce	ZnO:Y	ZnO:Eu
E_{gap} at RT (eV)	3.2658	3.2706	3.2658	3.2622

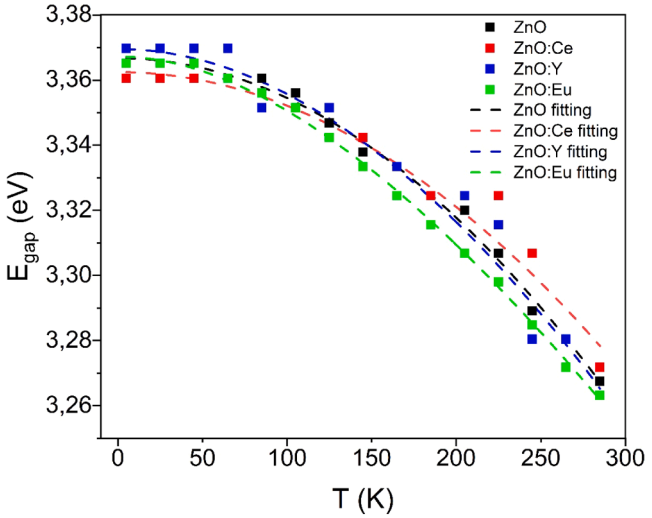

Fig. 9. Dots represent experimental data of near-band energy at different temperatures. The dashed line represents their Varshni's relation adjustment.

Table 3
Theoretical near-band edge of the samples at 0 K, calculated by Varshni's relation.

	ZnO	ZnO:Ce	ZnO:Y	ZnO:Eu
E_{gap} (0 K) (eV)	3.36676 ± 0.00124	3.36248 ± 0.00237	3.36957 ± 0.00381	3.36725 ± 0.00085

high crystallinity in all samples, with only slight (101) peak shifts attributable to surface-induced lattice strain. FESEM showed that plate-like ZnO nanosheets remained the dominant morphology, while HAADF-STEM and EDX mapping unambiguously revealed RE-rich secondary phases intimately decorating the ZnO surface. Band-gap measurements were unchanged, although RE modifiers altered ZnO's

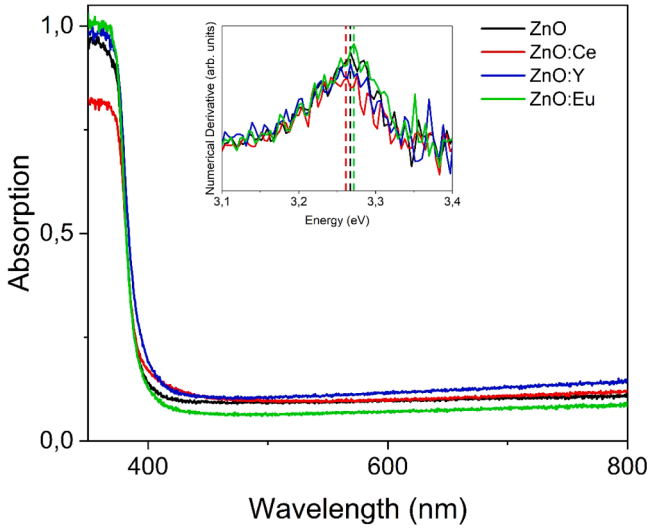

Fig. 10. Absorption plot of the samples. The inset represents the numerical derivative of the absorption spectrum. The maximum of the derivative, represented with a dashed vertical line, coincides with the near-band optical edge at RT. Pure ZnO and ZnO:Y have the same near-band edge and the vertical black line marks the same near-band edge for both.

Table 4
Numerical near-band edge obtained from the derivative of the absorption spectra.

	ZnO	ZnO:Ce	ZnO:Y	ZnO:Eu
E_{gap} at RT (eV)	3.2671	3.2621	3.2671	3.2718

absorption profile.

Photocatalytic degradation of methylene blue under solar-simulated irradiation demonstrated superior performance for all ZnO:RE samples compared to pure ZnO and TiO_2-P25, with ZnO:Ce achieving the highest rate constant (12.03×10^{-2} M·min^{-1}). PL quenching and TEM analyses linked this enhancement to reduced electron–hole recombination and efficient Ce^{4+}/Ce^{3+} redox cycling at the ZnO interface. BET surface-area measurements (Supporting Information) further support the role of increased active sites.

Together, these findings establish rare-earth surface decoration rather than lattice incorporation as a new design strategy for ZnO-based

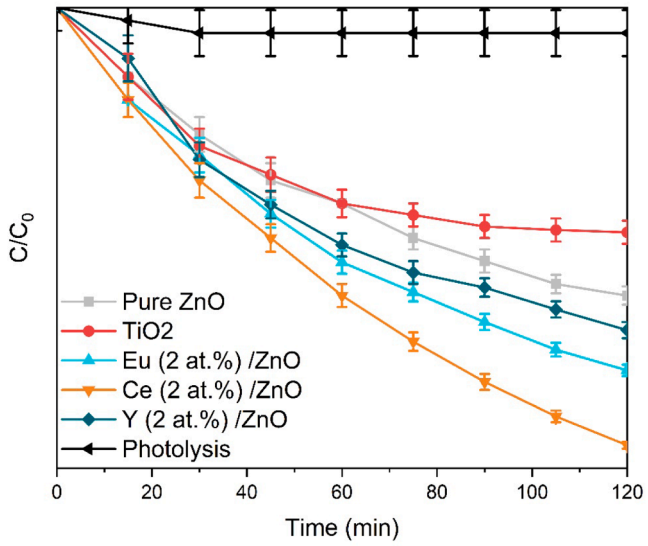

Fig. 11. Variation of MB concentration against reaction time in the absence and presence of ZnO, ZnO:RE and P25 photocatalysts.

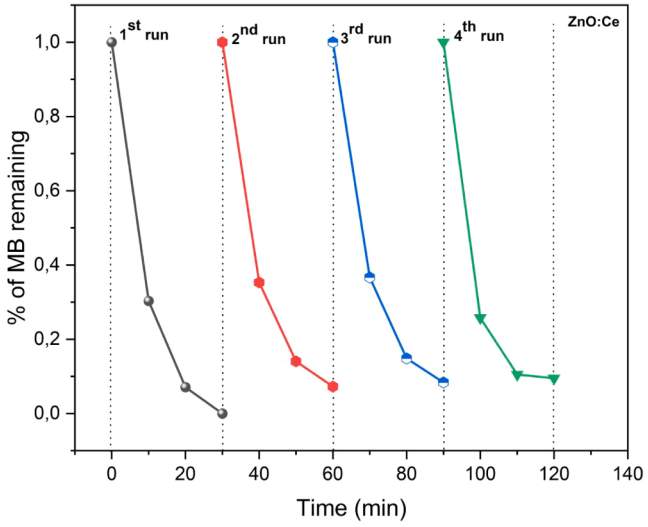

Fig. 12. Recycling experiments of photodegradation of MB.

photocatalysts, combining rapid, scalable synthesis, realistic solar-driven testing, and in-depth nanoscale and post-use characterization to deliver robust, high-efficiency systems for environmental remediation.

CRediT authorship contribution statement

Otman Bazta: Writing – original draft, Methodology, Investigation, Conceptualization. **Juan Francisco Ramos-Justicia:** Investigation, Data curation. **Ana Urbieta:** Investigation, Formal analysis, Conceptualization. **Susana Trasobares:** Visualization, Investigation. **Paloma Fernández:** Validation, Investigation, Data curation. **Jose Juan Calvino:** Supervision, Investigation, Funding acquisition. **Ana Belén Hungría:** Supervision, Funding acquisition, Formal analysis, Data curation.

Declaration of competing interest

- The authors declare that there is no conflict of interest.
- The authors declare that they have no known competing financial interests or personal relationships that could have appeared to influence the work reported in this paper.

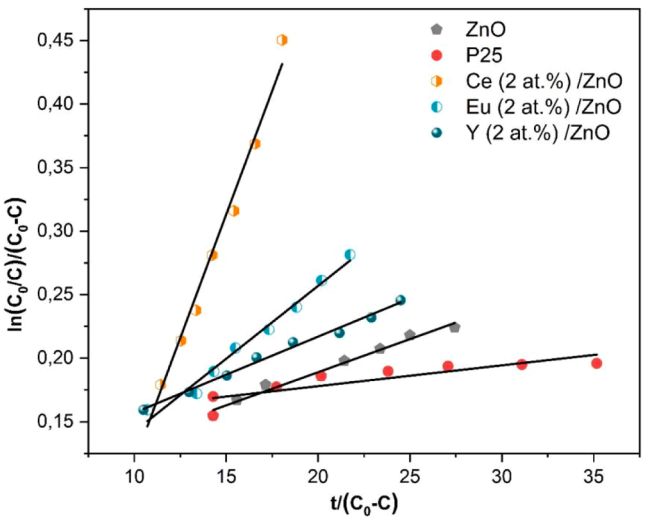

Fig. 13. Langmuir-Hinshelwood plots of MB photo-discoloration with presence of pure ZnO, ZnO:RE and P25 photocatalysts.

Table 5
Numerical values of apparent constant estimated using L-H model.

Sample	k (M. min^{-1})
ZnO	9.57×10^{-3}
P25	5.83×10^{-3}
Eu (2 at. %)/ZnO	8.53×10^{-2}
Y (2 at. %)/ZnO	8.2×10^{-2}
Ce (2 at. %)/ZnO	12.03×10^{-2}

Acknowledgments

Grant PID2022–142312NB-I00 funded by MICIU/AEI/10.13039/501100011033 and by ERDF/EU. This work has been partially financed by UCM under project PR3/23–30813. J. F. Ramos-Justicia acknowledges financial support from UCM-Banco Santander (Programa de ayudas de Contratos Predoctorales CT15/23).

Supplementary materials

Supplementary material associated with this article can be found, in the online version, at doi:10.1016/j.surfin.2025.107657.

Data availability

Data will be made available on request.

References

[1] J. Zhang, K. Yu, Y. Yu, L.L. Lou, Z. Yang, J. Yang, S. Liu, Highly effective and stable Ag3PO4/WO3photocatalysts for visible light degradation of organic dyes, J. Mol. Catal. Chem. 391 (2014) 12–18, https://doi.org/10.1016/j.molcata.2014.04.010.
[2] Y.C. Liang, P.H. Wang, Enhancing the performance of Bi2O3–ZnO semiconductor bilayers for photoelectrochemical electrodes by strategically engineering oxygen vacancies, J. Sci.:. Adv. Mater. Devic. 10 (2025), https://doi.org/10.1016/j.jsamd.2025.100895.
[3] V. Mane, D. Dake, N. Raskar, R. Sonpir, E. Stathatos, B. Dole, A review on Bi2O3 nanomaterial for photocatalytic and antibacterial applications, Chem. Phys. Impact. 8 (2024), https://doi.org/10.1016/j.chphi.2024.100517.
[4] A.A. Ismail, A. El-Midany, E.A. Abdel-Aal, H. El-Shall, Application of statistical design to optimize the preparation of ZnO nanoparticles via hydrothermal technique, Mater. Lett. 59 (2005) 1924–1928, https://doi.org/10.1016/j.matlet.2005.02.027.

[5] A.H. Navidpour, B. Xu, M.B. Ahmed, J.L. Zhou, Immobilization of TiO2 and ZnO by facile surface engineering methods to improve semiconductor performance in photocatalytic wastewater treatment: a review, Mater. Sci. Semicond. Process. 179 (2024), https://doi.org/10.1016/j.mssp.2024.108518.

[6] I. Ahmad, R. Bousbih, A. Mahal, W.Q. Khan, M. Aljohani, M.A. Amin, N.N.A. Jafar, M.S. Jabir, H. Majdi, A.S. Alshomrany, M. Shaban, I. Ali, H. Bayahia, Recent progress in ZnO-based heterostructured photocatalysts: a review, Mater. Sci. Semicond. Process. 180 (2024), https://doi.org/10.1016/j.mssp.2024.108578.

[7] Y. Sun, W. Zhang, Q. Li, H. Liu, X. Wang, Preparations and applications of zinc oxide based photocatalytic materials, Adv. Sens. Energy. Mater. 2 (2023) 100069, https://doi.org/10.1016/j.asems.2023.100069.

[8] V. Mariyappillai, C. Shiyamala, T. Abisheik, M. Tiffany, V. Pandiyan, A. Senthilraja, M. Afzal, P. Barmavatu, K. Shanmugaraj, K. Balu, Zr-modified ZnO nanoparticles: optimized photocatalytic degradation and antibacterial efficiency for pollution control, Ceram. Int. (2025), https://doi.org/10.1016/j.ceramint.2025.02.402.

[9] S. Sun, X. Chang, X. Li, Z. Li, Synthesis of N-doped ZnO nanoparticles with improved photocatalytical activity, Ceram. Int. 39 (2013) 5197–5203, https://doi.org/10.1016/j.ceramint.2012.12.018.

[10] B. Subash, B. Krishnakumar, R. Velmurugan, M. Swaminathan, M. Shanthi, Synthesis of Ce co-doped Ag-ZnO photocatalyst with excellent performance for NBB dye degradation under natural sunlight illumination, Catal. Sci. Technol. 2 (2012) 2319–2326, https://doi.org/10.1039/c2cy20254a.

[11] C. Gomez-Solís, J.C. Ballesteros, L.M. Torres-Martínez, I. Juárez-Ramírez, L.A. Díaz Torres, M.Elvira Zarazua-Morin, S.W. Lee, Rapid synthesis of ZnO nano-corncobs from Nital solution and its application in the photodegradation of methyl orange, J. Photochem. Photobiol. Chem. 298 (2015) 49–54, https://doi.org/10.1016/j.jphotochem.2014.10.012.

[12] O. Altintas Yildirim, H. Arslan, S. Sönmezoğlu, Facile synthesis of cobalt-doped zinc oxide thin films for highly efficient visible light photocatalysts, Appl. Surf. Sci. 390 (2016) 111–121, https://doi.org/10.1016/j.apsusc.2016.08.069.

[13] R. Nasser, W.B.H. Othmen, H. Elhouichet, M. Férid, Preparation, characterization of Sb-doped ZnO nanocrystals and their excellent solar light driven photocatalytic activity, Appl. Surf. Sci. 393 (2017) 486–495, https://doi.org/10.1016/j.apsusc.2016.09.158.

[14] R. Rooydell, S. Brahma, R.C. Wang, M.R. Modaberi, F. Ebrahimzadeh, C.P. Liu, Cu doped ZnO nanorods with controllable Cu content by using single metal organic precursors and their photocatalytic and luminescence properties, J. Alloys. Compd. 691 (2017) 936–945, https://doi.org/10.1016/j.jallcom.2016.08.324.

[15] I. Ahmad, M.Q. Alfaifi, S. Ben Ahmed, M.M. Abduljawad, Y.A. Alassmy, S. A. Alshuhri, T.L. Tamang, Strategies for optimizing sunlight conversion in semiconductor photocatalysts: a review of experimental and theoretical insights, Int. J. Hydrog. Energy 96 (2024) 1006–1066, https://doi.org/10.1016/j.ijhydene.2024.11.388.

[16] H. Wang, L. Zhang, Z. Chen, J. Hu, S. Li, Z. Wang, J. Liu, X. Wang, Semiconductor heterojunction photocatalysts: design, construction, and photocatalytic performances, Chem. Soc. Rev. 43 (2014) 5234–5244, https://doi.org/10.1039/c4cs00126e.

[17] E.M. Seftel, M.C. Puscasu, M. Mertens, P. Cool, G. Carja, Fabrication of CeO2/LDHs self-assemblies with enhanced photocatalytic performance: a case study on ZnSn-LDH matrix, Appl. Catal. B 164 (2015) 251–260, https://doi.org/10.1016/j.apcatb.2014.09.035.

[18] S.J.A. Moniz, S.A. Shevlin, D.J. Martin, Z.X. Guo, J. Tang, Visible-light driven heterojunction photocatalysts for water splitting-a critical review, Energy. Env. Sci. 8 (2015) 731–759, https://doi.org/10.1039/c4ee03271c.

[19] L. Zhao, J. Jia, Z. Yang, J. Yu, A. Wang, Y. Sang, W. Zhou, H. Liu, One-step synthesis of CdS nanoparticles/MoS2 nanosheets heterostructure on porous molybdenum sheet for enhanced photocatalytic H2 evolution, Appl. Catal. B 210 (2017) 290–296, https://doi.org/10.1016/j.apcatb.2017.04.003.

[20] S.M. ul Hassan, W. Akram, A. Noureen, F. Ahmed, A. Hassan, A. Ullah, Advances in transition metals and rare earth elements doped ZnO as thermoluminescence dosimetry material, Radiat. Phys. Chem. 223 (2024), https://doi.org/10.1016/j.radphyschem.2024.111929.

[21] S. Karakaya, L. Kaba, Photocatalytic activity of rare earth elements (Gd and ce) co-doped ZnO nanostructured films, Ceram. Int. 50 (2024) 30743–30753, https://doi.org/10.1016/j.ceramint.2024.05.374.

[22] S. Selvaraj, M.K. Mohan, M. Navaneethan, S. Ponnusamy, C. Muthamizhchelvan, Synthesis and photocatalytic activity of Gd doped ZnO nanoparticles for enhanced degradation of methylene blue under visible light, Mater. Sci. Semicond. Process. 103 (2019), https://doi.org/10.1016/j.mssp.2019.104622.

[23] W. Raza, S.M. Faisal, M. Owais, D. Bahnemann, M. Muneer, Facile fabrication of highly efficient modified ZnO photocatalyst with enhanced photocatalytic, antibacterial and anticancer activity, RSC. Adv. 6 (2016) 78335–78350, https://doi.org/10.1039/c6ra06774c.

[24] H. Shi, P. Zhang, S.S. Li, J.B. Xia, Magnetic coupling properties of rare-earth metals (Gd, Nd) doped ZnO: first-principles calculations, J. Appl. Phys. 106 (2009), https://doi.org/10.1063/1.3176490.

[25] N. Kaneva, A. Bojinova, K. Papazova, D. Dimitrov, Photocatalytic purification of dye contaminated sea water by lanthanide (La 3+, Ce 3+, Eu 3+) modified ZnO, Catal. Today 252 (2015) 113–119, https://doi.org/10.1016/j.cattod.2014.12.008.

[26] U. Pratomo, N. Fransisca, M.D. Adzani, I. Irkham, A.P. Sulaeman, D.R. Eddy, J. Y. Mulyana, I. Primadona, Doping of rare earth element: the effects in elevated physical and optical properties of ZnO, Talanta. Open. 11 (2025), https://doi.org/10.1016/j.talo.2025.100411.

[27] J.C. Sin, S.M. Lam, K.T. Lee, A.R. Mohamed, Fabrication of erbium-doped spherical-like ZnO hierarchical nanostructures with enhanced visible light-driven photocatalytic activity, Mater. Lett. 91 (2013) 1–4, https://doi.org/10.1016/j.matlet.2012.09.049.

[28] L.V. Trandafilović, D.J. Jovanović, X. Zhang, S. Ptasińska, M.D. Dramićanin, Enhanced photocatalytic degradation of methylene blue and methyl orange by ZnO:eu nanoparticles, Appl. Catal. B 203 (2017) 740–752, https://doi.org/10.1016/j.apcatb.2016.10.063.

[29] Y. Zong, Z. Li, X. Wang, J. Ma, Y. Men, Synthesis and high photocatalytic activity of Eu-doped ZnO nanoparticles, Ceram. Int. 40 (2014) 10375–10382, https://doi.org/10.1016/j.ceramint.2014.02.123.

[30] O. Bazta, A. Urbieta, S. Trasobares, J. Piqueras, P. Fernández, M. Addou, J. J. Calvino, A.B. Hungría, In-depth structural and optical analysis of ce-modified zno nanopowders with enhanced photocatalytic activity prepared by microwave-assisted hydrothermal method, Catalysts 10 (2020), https://doi.org/10.3390/catal10050551.

[31] J.C. Sin, S.M. Lam, K.T. Lee, A.R. Mohamed, Preparation and photocatalytic properties of visible light-driven samarium-doped ZnO nanorods, Ceram. Int. 39 (2013) 5833–5843, https://doi.org/10.1016/j.ceramint.2013.01.004.

[32] M. Faraz, F.K. Naqvi, M. Shakir, N. Khare, Synthesis of samarium-doped zinc oxide nanoparticles with improved photocatalytic performance and recyclability under visible light irradiation, New. J. Chem. 42 (2018) 2295–2305, https://doi.org/10.1039/c7nj03927a.

[33] A.T. Ravichandran, R. Karthick, A.R. Xavier, R. Chandramohan, S. Mantha, Influence of Sm doped ZnO nanoparticles with enhanced photoluminescence and antibacterial efficiency, J. Mater. Sci. 28 (2017) 6643–6648, https://doi.org/10.1007/s10854-017-6355-2.

[34] M. Rezaei, A. Habibi-Yangjeh, Simple and large scale refluxing method for preparation of Ce-doped ZnO nanostructures as highly efficient photocatalyst, Appl. Surf. Sci. 265 (2013) 591–596, https://doi.org/10.1016/j.apsusc.2012.11.053.

[35] I.A. Siddiquey, T. Furusawa, M. Sato, K. Honda, N. Suzuki, Control of the photocatalytic activity of TiO2 nanoparticles by silica coating with polydiethoxysiloxane, Dyes. Pigm. 76 (2008) 754–759, https://doi.org/10.1016/j.dyepig.2007.01.020.

[36] M.A. Hernández-Carrillo, R. Torres-Ricárdez, M.F. García-Mendoza, E. Ramírez-Morales, L. Rojas-Blanco, L.L. Díaz-Flores, G.E. Sepúlveda-Palacios, F. Paraguay-Delgado, G. Pérez-Hernández, Eu-modified ZnO nanoparticles for applications in photocatalysis, Catal. Today 349 (2020) 191–197, https://doi.org/10.1016/j.cattod.2018.04.060.

[37] J.R. Mora, G. Flores-Carrasco, H. Juárez, M. Pacio, M. de la L. Olvera, M. E. Rabanal, Ce-doped ZnO nanonails synthesized by a simple thermal evaporation method for photocatalytic degradation, Opt. Mater. 157 (2024), https://doi.org/10.1016/j.optmat.2024.116156.

[38] A.H. Ajil, N.M. Ahmed, F.K. Yam, Z.U. Zango, I.A. Wadi, A.M. Binzowaimil, O. Aldaghri, K.H. Ibnaouf, H. Cabrera, Enhancing Methyl Orange Degradation with Laser-Generated ZnO and Ce-Doped ZnO Nanoparticles, Appl. Sci. 13 (2023), https://doi.org/10.3390/app132111857.

[39] M. Wang, E.J. Kim, S. Kim, J.S. Chung, I.K. Yoo, E.W. Shin, S.H. Hahn, C. Park, Optical and structural properties of sol-gel prepared MgZnO alloy thin films, Thin. Solid. Films. 516 (2008) 1124–1129, https://doi.org/10.1016/j.tsf.2007.05.039.

[40] O. Bazta, A. Urbieta, J. Piqueras, P. Fernández, M. Addou, J.J. Calvino, A. B. Hungría, Influence of yttrium doping on the structural, morphological and optical properties of nanostructured ZnO thin films grown by spray pyrolysis, Ceram. Int. (2018), https://doi.org/10.1016/J.CERAMINT.2018.12.178.

[41] A. Qasem, M.S. Mostafa, H.A. Yakout, M. Mahmoud, E.R. Shaaban, Determination of optical bandgap energy and optical characteristics of Cd30Se50S20 thin film at various thicknesses, Opt. Laser. Technol. 148 (2022), https://doi.org/10.1016/j.optlastec.2021.107770.

[42] A.N. Ökte, Characterization and photocatalytic activity of Ln (La, Eu, Gd, Dy and Ho) loaded ZnO nanocatalysts, Appl. Catal. Gen. 475 (2014) 27–39, https://doi.org/10.1016/j.apcata.2014.01.019.

[43] J. Lin, J.C. Yu, D. Lo, S.K. Lam, Photocatalytic activity of rutile Ti1-xSnxO2 solid solutions, J. Catal. 183 (1999) 368–372, https://doi.org/10.1006/jcat.1999.2409.

[44] P. Jara, R. Fernández-Jiménez, A. Ferreiro, A. Urbieta, M.E. Rabanal, P. Fernández, Morphological, structural and luminescent characterization of Nd-doped ZnO nano- and microstructures grown by vapor-solid method, Mater. Sci. Eng. 299 (2024), https://doi.org/10.1016/j.mseb.2023.116941.

[45] A. Derri, M. Guezzoul, A. Mokadem, A. Ouerdane, K.B. Bensassi, M. Bouslama, B. Kharoubi, E. Hameurlaine, Insight into the photoluminescence and morphological characteristics of transition metals (TM = Mn, Ni, Co, Cu)-doped ZnO semiconductor: a comparative study, Opt. Mater. (Amst) 145 (2023), https://doi.org/10.1016/j.optmat.2023.114467.

[46] A. Urbieta, R. Del Campo, R. Pérez, P. Fernández, J. Piqueras, Luminescence and waveguiding behavior in Tb doped ZnO micro and nanostructures, J. Alloys. Compd. 610 (2014) 416–421, https://doi.org/10.1016/j.jallcom.2014.05.007.

[47] C. Boemare, T. Monteiro, M.J. Soares, J.G. Guilherme, E. Alves, Photoluminescence studies in ZnO samples, 2001.

[48] A. Galdámez-Martinez, G. Santana, F. Güell, P.R. Martínez-Alanis, A. Dutt, Photoluminescence of zno nanowires: a review, Nanomaterials 10 (2020), https://doi.org/10.3390/nano10050857.

[49] A.A. Sokol, S.A. French, S.T. Bromley, C.R.A. Catlow, H.J.J. Van Dam, P. Sherwood, Point defects in ZnO. Faraday Discuss, 2007, pp. 267–282, https://doi.org/10.1039/b607406e.

[50] J.L. Lyons, J.B. Varley, D. Steiauf, A. Janotti, C.G. Van De Walle, First-principles characterization of native-defect-related optical transitions in ZnO, J. Appl. Phys. 122 (2017), https://doi.org/10.1063/1.4992128.

[51] T. Torchynska, B. El Filali, J.A. Jaramillo Gomez, G. Polupan, J.L. Ramírez García, L. Shcherbyna, Raman scattering, emission, and deep defect evolution in ZnO: in thin films, J. Vac. Sci. Technol. A 38 (2020).
[52] F. Pavón, A. Urbieta, P. Fernández, Characterization, Luminescence and Optical Resonant Modes of Eu-Li Co-Doped ZnO Nano- and Microstructures, Appl. Sci. 12 (2022), https://doi.org/10.3390/app12146948.
[53] A. Urbieta, J.J. Calvino, M. Addou, P. Fernández, A.B. Hungría, O. Bazta, J. Piqueras, Influence of yttrium doping on the structural, morphological and optical properties of nanostructured ZnO thin films grown by spray pyrolysis, Ceram. Int. 45 (2018) 6842–6852, https://doi.org/10.1016/j.ceramint.2018.12.178.
[54] Y.P. Varshni, Temperature dependence of the energy gap in semiconductors, 1967.
[55] D.K. Sharma, S. Shukla, K.K. Sharma, V. Kumar, A review on ZnO: fundamental properties and applications. Mater Today Proc, Elsevier Ltd, 2020, pp. 3028–3035, https://doi.org/10.1016/j.matpr.2020.10.238.
[56] J.Pawlak Jarosiński, S.K.J. Al-Ani, Inverse logarithmic derivative method for determining the energy gap and the type of electron transitions as an alternative to the Tauc method, Opt. Mater. 88 (2019) 667–673, https://doi.org/10.1016/j.optmat.2018.12.041.
[57] N. Moslehnejad, M. Jahangiri, F. Vafaee, M. Salavati-Niasari, Synthesis and characterization of ZnO–Ce nanophotocatalyst and their application for the removal of dye (Reactive red 198) by degradation process: kinetics, thermodynamics and experimental design, Int. J. Hydrog. Energy 47 (2022) 23980–23993, https://doi.org/10.1016/j.ijhydene.2022.05.189.
[58] Y.D.R. De Mimérand, K. Li, C. Zhou, X. Jin, X. Hu, Y. Chen, J. Guo, Functional Supported ZnO/Bi2MoO6Heterojunction Photocatalysts with 3D-Printed Fractal Polymer Substrates and Produced by Innovative Plasma-Based Immobilization Methods, ACS. Appl. Mater. Interfaces. 12 (2020) 43138–43151, https://doi.org/10.1021/acsami.0c12286.
[59] I. Ahmad, S. Shukrullah, M.Y. Naz, H.N. Bhatti, M. Ahmad, E. Ahmed, S. Ullah, M. Hussien, Recent progress in rare earth oxides and carbonaceous materials modified ZnO heterogeneous photocatalysts for environmental and energy applications, J. Env. Chem. Eng. 10 (2022), https://doi.org/10.1016/j.jece.2022.107762.
[60] Q. Zhang, X. Zhao, L. Duan, H. Shen, R. Liu, Controlling oxygen vacancies and enhanced visible light photocatalysis of CeO2/ZnO nanocomposites, J. Photochem. Photobiol. Chem. 392 (2020), https://doi.org/10.1016/j.jphotochem.2019.112156.
[61] P. Rodionovs, J. Grabis, ZnO photocatalysts modified with Eu2O3 and Sm2O3, Key. Eng. Mater. 850 (2020) 35–40.
[62] M.A. Hasnat, M.M. Uddin, A.J.F. Samed, S.S. Alam, S. Hossain, Adsorption and photocatalytic decolorization of a synthetic dye erythrosine on anatase TiO2 and ZnO surfaces, J. Hazard. Mater. 147 (2007) 471–477, https://doi.org/10.1016/j.jhazmat.2007.01.040.
[63] S.J. Xia, F.X. Liu, Z.M. Ni, J.L. Xue, P.P. Qian, Layered double hydroxides as efficient photocatalysts for visible-light degradation of Rhodamine B, J. Colloid. Interface. Sci. 405 (2013) 195–200, https://doi.org/10.1016/j.jcis.2013.05.064.